ADVANCED MATERIALS
www.advmat.de

Initiator-Free Supramolecular Zwitterionic Gels for Skin-Inspired Soft Iontronics

Buguang Zhou, Yinghui Li, Yue Chen, Jiecong Li, Jiansheng Guo, Can Gao, Zixuan Zhang,* and Chengkuo Lee**

Conventional synthetic skin for intelligent soft robotics typically relies on thermally or UV-initiated polymerization, making initiator-free rapid gelation a persistent challenge. Here, a supramolecular Lewis acid–base gelation strategy that enables facile, initiator- and crosslinker-free synthesis of polyzwitterionic gels is presented. Strong hydrogen bonding between urea (hydrogen bond donor, HBD) and the zwitterionic moieties of 2-methacryloyloxyethyl phosphorylcholine (MPC; polymerizable zwitterionic hydrogen bond acceptor, PZHBA) drives spontaneous polymerization, establishing a general platform for zwitterionic gelation in deep eutectic solvents (DESs), such as choline chloride (ChCl) and urea. Inspired by the structural and ionic complexity of human skin, zwitterionic supramolecular eutectogel (ZSE) is designed via copolymerization of N-acryloyl glycinamide (NAGA) and MPC in DES, yielding a bioinspired ion–hydrogen bond dynamic network. These gels exhibit tunable mechanical properties, including an ultralow Young's modulus (5–180 kPa), and exceptionally high ionic conductivity (2 S·m^{-1}), which arises from the solvation of zwitterionic groups. The dynamic supramolecular network also imparts recyclability and intrinsic self-adhesion. ZSEs can be continuously spun into highly sensitive strain sensors with environmental robustness for integration into textiles. Additionally, bio-optimized gel patches demonstrate excellent antibacterial activity and biocompatibility. This work offers a sustainable and versatile synthetic platform for next-generation soft iontronics and bioinspired human-machine interfaces.

1. Introduction

In recent years, various types of gels have shown broad application potential in soft iontronics,[1] self-powered sensors,[2,3] and human-machine interaction fields.[4,5] Particularly, ionic gels (ionogels) and eutectic gels (eutectogels), as promising ionic conductors in smart sensing and flexible iontronic devices, have gradually become research hotspots.[6,7] Compared with hydrogels, they possess significant advantages such as non-volatile solvents, excellent thermal stability, and higher ionic conductivity.[8–10] While polymerizing eutectogels leverage DESs for greener fabrication compared to ionic liquids, existing synthesis strategies often rely on initiators,[11,12] crosslinkers, or energy-intensive processes,[13] introducing safety risks, impurities, and environmental concerns. The intrinsic catalytic properties of DESs—modulating reactant polarization states to accelerate reactions—hint at untapped potential for simplifying monomer gelation processes.[14] However, eliminating initiators and crosslinkers while maintaining rapid gelation remains a critical challenge in designing biocompatible and sustainable supramolecular polymeric gels.

Zwitterionic polymers offer unique and significant opportunities for constructing bioinspired ionic interfaces, owing to their exceptional antifouling properties, excellent biocompatibility, and effective simulation of ion transport mechanisms in biological phospholipids.[15–17] The high polarity of their side chains significantly enhances the reactivity of monomers,[18] while the ion-dipole interactions between

B. Zhou, Y. Li, Y. Chen, J. Li, J. Guo
Key Laboratory of Textile Science & Technology
Ministry of Education
College of Textiles
Donghua University
Shanghai 201620, China
E-mail: jsguo@dhu.edu.cn

Z. Zhang, C. Lee
Department of Electrical & Computer Engineering
National University of Singapore
Singapore 117583, Singapore
E-mail: elezzix@nus.edu.sg; elelc@nus.edu.sg

The ORCID identification number(s) for the author(s) of this article can be found under https://doi.org/10.1002/adma.202514037

DOI: 10.1002/adma.202514037

Z. Zhang, C. Lee
Center for Intelligent Sensors and MEMS
National University of Singapore
Singapore 117583, Singapore

C. Lee
Research Platform for Biomedical and Health Technology
National University of Singapore (Suzhou) Research Institute
Suzhou 215123, China

C. Gao
School of Textile and Clothing
Nantong University
Nantong 226019, China

side groups facilitate salt dissociation within the system[19,20] and serve as conduction channels for physiologically relevant ions. Zwitterionic phosphorylcholine (PC), by virtue of its outstanding water absorption capacity and ionic conductive characteristics, plays crucial physiological roles in the head groups of phospholipids within skin cell membranes.[21] However, conventional zwitterionic hydrogels commonly suffer from insufficient mechanical strength and excessive hydrophilicity, which limit their practical applications in skin-mimetic high-strength sensing materials.[22,23] In comparison, natural skin architecture achieves elastic deformation through elastin networks and resists large strains via rigid collagen fiber bundles, demonstrating superior mechanical synergy.[24,25] Recent studies have demonstrated that eutectogels based on dynamic polymer networks can achieve a favorable balance between strength and ductility, suggesting that incorporating zwitterionic monomers into deep eutectic solvent systems holds promise for developing skin-like ionic materials with both high mechanical elasticity and toughness.

Herein, we demonstrate a self-initiated strategy for synthesizing ZSE that emulates skin's dual attributes of ionic sensing and mechanical adaptability. By exploiting Lewis acid-base interactions between DES components and zwitterionic monomers, we enable rapid thermal gelation without initiators or crosslinkers. The resultant network combines hydrogen-bonded microdomains for elasticity with ion-dipole interactions for ionic conductivity, addressing the mechanical limitations of zwitterionic polymers while preserving their dynamic reconfigurability. Comparative analysis with recent research (Figure S1a and Table S1, Supporting Information; **Figure 1**a,d) reveals three distinctive synthetic material innovations and performance merits integrated in this gel: 1) Polymerization and gelation of zwitterionic monomers without initiators or crosslinkers, enabled by Lewis acid-base interactions. 2) Enhancement of elasticity and toughness through the introduction of hydrogen-bonding microdomains. 3) Promotion of ionic migration via zwitterionic polyelectrolyte dissociation in DESs. The ZSE exhibits skin-like multifunctionality while supporting recyclable processing via reversible network dissociation. As wearable sensors, they can achieve reliable multimodal sensing, electrophysiological monitoring, and human-machine interaction.

2. Results and Discussion

2.1. Synthesis Concept and Gelation Mechanism

Human skin, as the largest organ in the body, possesses a 3D network of elastic fibers and collagen, providing high elasticity, remarkable deformability, self-healing properties, and sensory neuron integration that detects and transmits stimuli through ion movement (Figure S1b, Supporting Information).[26,27] Recently, synthetic ionic skins and filaments with skin-like properties have drawn significant attention in wearable sensing, medical monitoring, and human-machine interactions.[28–30] Ionic eutectogels, a novel class of soft materials, emulate human skin's architecture and functionality.[27,31]

Inspired by these features, we developed ZSE with high ion-regulation capability and tunable viscoelasticity, enabling real-time motion and physiological signal monitoring (Figure 1c,e). ChCl and urea were chosen as the hydrogen bond acceptor (HBA) and HBD, respectively, due to their biocompatibility and cost-effectiveness. These components were mixed to form a stable DES. PZHBA (MPC) and polymerizable hydrogen-bond donor (PHBD, NAGA) were dissolved in the DES, and after continuous heating, a transparent precursor solution of polymerizable deep eutectic solvent (PDES) was obtained. Furthermore, the versatility of this methodology derives from the substitution of components with analogous physical properties, enabling versatile synthesis strategies provided that the HBD and PZHBA motifs are retained (Figure 1b). The ZSE was successfully fabricated through spontaneous one-pot polymerization, integrating zwitterionic polymer chains and dual hydrogen-bonded dynamic domains without the need for additional initiators or crosslinkers (Figure S2a, Supporting Information).

To investigate the gelation mechanism, comparative studies of monomer-based deep eutectic systems showed that gelation was largely independent of NAGA. Replacing the DES with water or dimethyl sulfoxide (DMSO) prevented gelation, even after 24 h at 80 °C (Figure S2b,c, Supporting Information). We hypothesize that gelation originates from interactions between MPC and hydrogen bond donors/acceptors in the DES, promoting polymerization and forming supramolecular interactions with the solvent. Time-dependent rheological tests (**Figure 2**a) revealed that a 25 wt% MPC–DES system required ≈25 min for gelation at 80 °C, with the gelation time dependent on MPC concentration and temperature (Figure S3a,b, Supporting Information). No gelation occurred at room temperature (Figure S3c, Supporting Information), confirming the temperature dependence of the gelation process. Rheological measurements of the polymerized MPC gel (Figure S4, Supporting Information) demonstrated typical elastic behavior with storage modulus (G′) greater than loss modulus (G″) across all frequencies for a 30 wt% gel. At 15 wt%, G′ and G″ decreased but remained in the gel range, confirming gel characteristics.

To explore structural changes, MPC (25 wt%) was polymerized with DES at 80 °C for at least 1 h, dialyzed, and freeze-dried (MPC@DES). Fourier transform infrared spectroscopy (FTIR, Figure 2b) revealed the disappearance of the —C—N^+— peak at 1302 cm^{-1}, indicative of enhanced electrostatic interactions between —$N^+(CH_3)_3$ and —PO_4^- post-polymerization.[32] Other peaks, such as C═C stretching at 1600–1660 cm^{-1}, also vanished, and the ester carbonyl peak shifted.[33] Raman spectroscopy confirmed these findings (Figure 2c).[34] ^{1}H nuclear magnetic resonance spectra (^{1}H NMR, Figure S5, Supporting Information) showed that the methacrylate proton resonances merged into a methylene envelope, indicating polymerization. Gel permeation chromatography (GPC, Figure S6, Supporting Information) revealed an average molecular weight (M_w) of ≈1.5 × 10^5 Da for MPC@DES, corresponding to ≈510 repeating units per chain, confirming initiator-free thermal polymerization.

Further investigation revealed interactions between MPC's PC group and DES components. ^{1}H NMR (Figure 2d) indicated that the —NH_2 protons in urea shifted downfield in the PC–Urea system, suggesting dominant interactions between PC's phosphate groups and urea's amino groups. In contrast, interactions between PC and ChCl showed minimal changes (Figure S7d, Supporting Information), indicating weak hydrogen bonding. Density functional theory (DFT) calculations (Figure 2e) revealed a

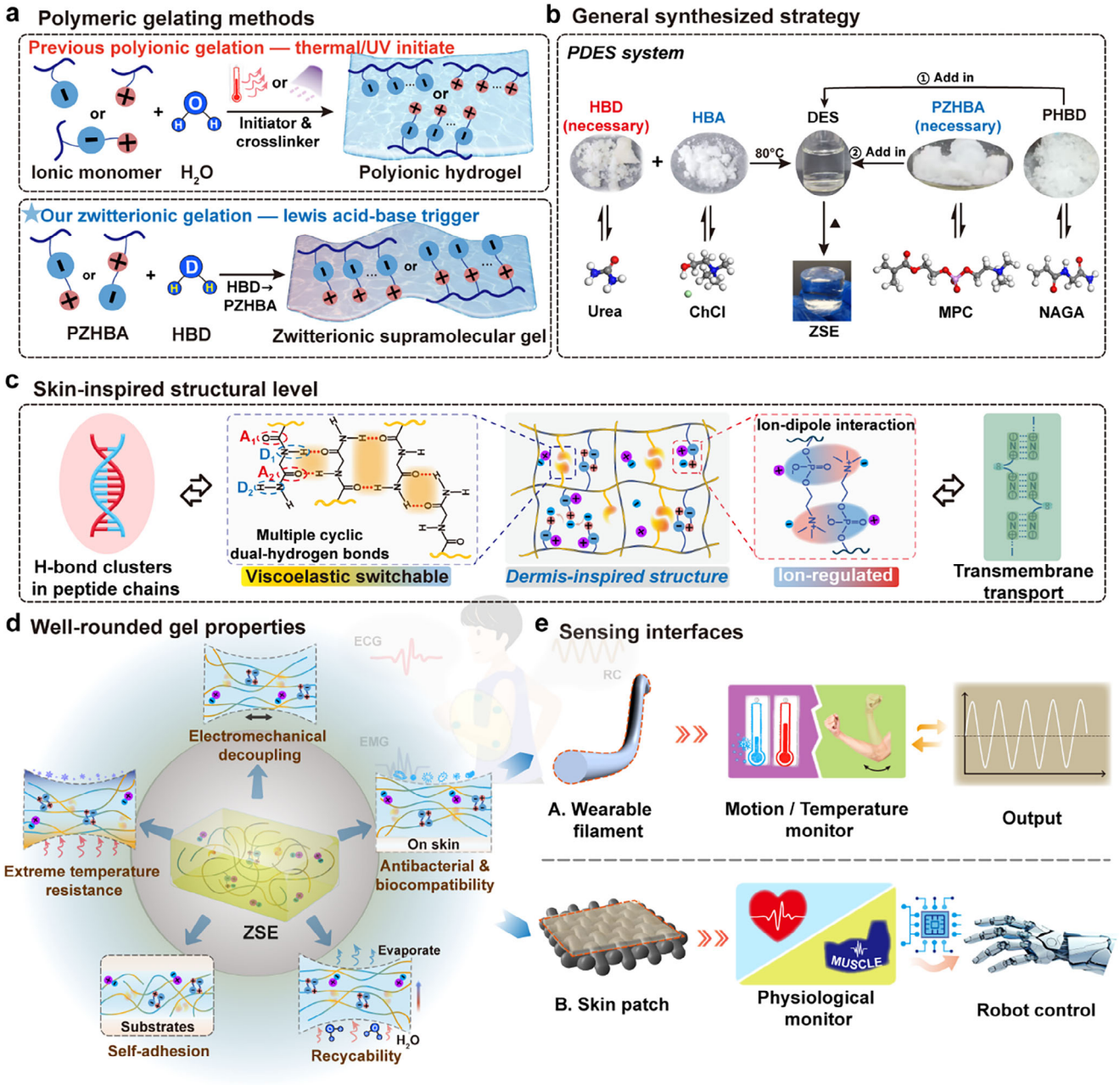

Figure 1. A universal strategy for initiator free zwitterionic gels and the synthesis and sensing design concept of skin-inspired ZSE. a) Polymeric ionic gel synthesis schematic of conventional and our special gelating method. b) General gelation strategy and its chemical components in the PDES precursor solution, including DES, PZHBA, and PHBD constituents. c) Skin-inspired physically supramolecular eutectogel with multi-cyclic dual hydrogen-bonded domains (acceptor (A), donor (D)) and structural interactions involving ion-dipole and dipole-dipole forces. Biomimetic design of hydrogen bond clusters and Transmembrane Channels, respectively. d) Schematic showing representative properties of ZSE, including electromechanical decoupling, self-adhesion, extreme temperature resistance, antibacterial and biocompatibility, and recyclability. e) Based on this biomimetic concept and its well-rounded performance, the switchable sensing interfaces fabricated by ZSE can achieve information interaction between humans and machines. It can realize multi-modal monitoring of the body surface and real-time control of the robot hand through sensing methods such as strain, temperature, or physiological signals.

larger electrostatic potential difference in the PC–Urea system, reflecting enhanced electron cloud polarization induced by urea. Orbital energy level analysis (Figure S8b, Supporting Information) revealed that MPC–Urea interactions increased reactivity, while MPC–ChCl stabilized the system, confirming urea's role as a hydrogen-bond donor driving MPC polymerization.[35,36] According to the Lewis Acid-Base Pair Theory, urea's strengthened hydrogen-bond donor behavior enhances the Lewis acidity of MPC's polar side chains. This forms charge-transfer complexes that destabilize conjugated double bonds via uneven electron

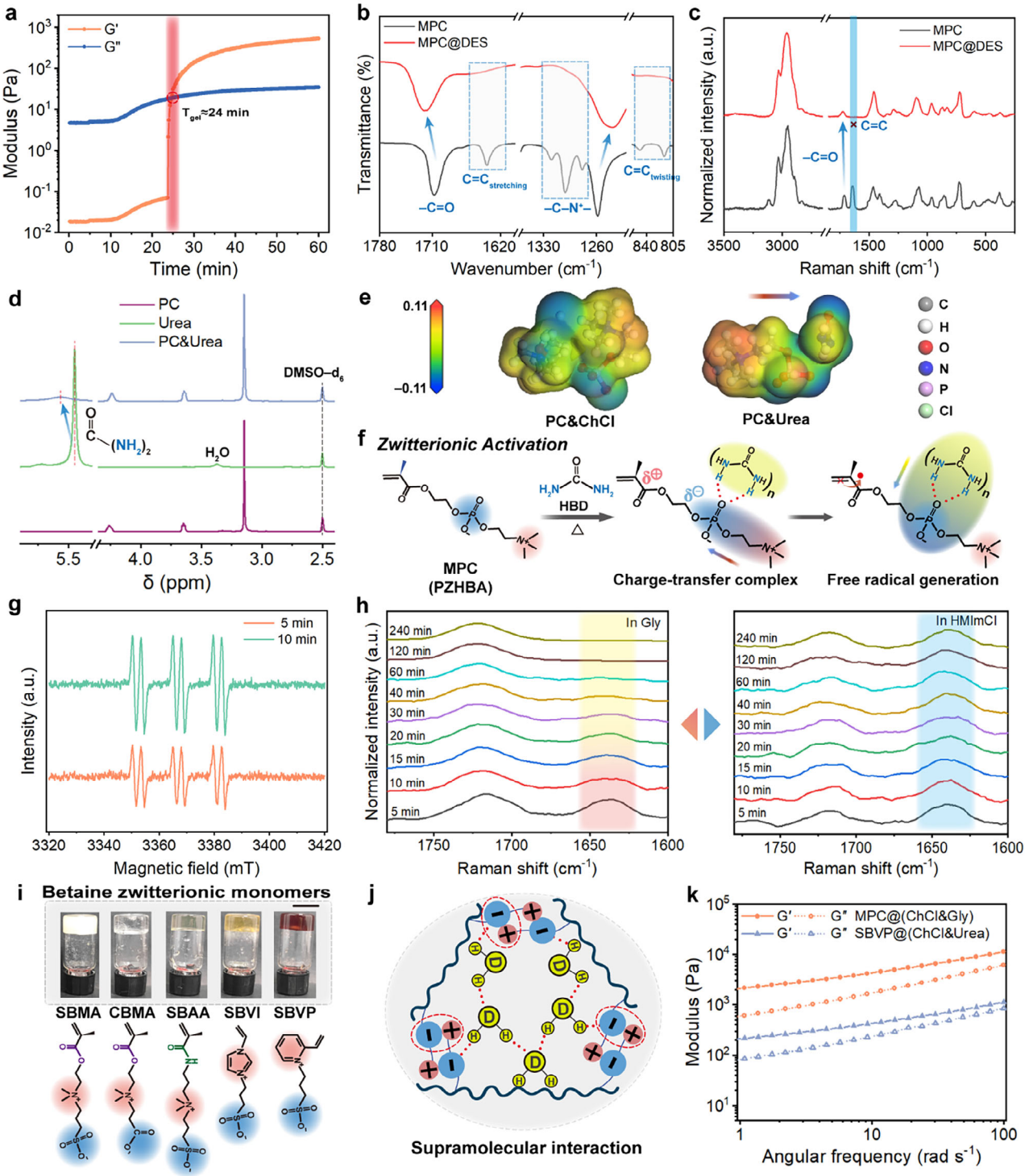

Figure 2. Lewis acid-base gelation mechanism of the zwitterionic deep eutectic system. a) Rheological monitoring of MPC gelation in DES (25 wt%). The intersection of storage modulus (G') and loss modulus (G'') curves marks the gel point. b) ATR–FTIR spectra of MPC monomer and MPC@DES in the ranges of 1800–1600, 1360–1220, and 860–800 cm^{-1}. c) Raman spectra of MPC monomer and MPC@DES. d) ^{1}H NMR spectra of PC, urea, and PC&Urea. e) DFT–optimized structures and electrostatic potential surfaces of PC&ChCl and PC&Urea. f) Proposed activation mechanism of MPC under hydrogen-bond donors (urea). g) EPR spectra of MPC@DES with PBN adduction under 80 °C for 20 min. Three twin peaks express the signals of monomer radicals. h) In situ Raman spectra tracking MPC polymerization in Gly and HMImCl. i) Photographs of pure zwitterionic gels derived from SBMA, CBMA, SBAA, SBVI, and SBVP monomers, alongside their chemical structures (scale bar: 1 cm). j) Mechanistic diagram of supramolecular ionic/hydrogen-bonding interactions after gelation. k) Rheological properties of gels polymerized using alternative zwitterionic monomer SBVP or DES (ChCl&Gly) (concentration: 25 wt%).

distribution, facilitating radical generation and subsequent self-polymerization (Figure 2f).

Radical scavenger studies confirmed the involvement of radicals in the gelation process. The addition of 1,1-diphenyl-2-picrylhydrazyl (DPPH) completely inhibited gelation in the PDES system. Since DES served as the medium with Gly as HBD, and no other radical-prone components were present, conventional free-radical polymerization (FRP) can be ruled out. Based on existing theories and research, this polymerization reaction can be confidently identified as a free-radical process, as the cationic pathway has been proven to be infeasible.[37] UV–vis spectroscopy revealed slight discoloration in the DPPH→DES system containing MPC (Figure S9a,b, Supporting Information), while hydroquinone (HQ)-containing MPC@DES showed yellow coloration due to redox reactions (Figure S9c, Supporting Information), indicating a radical polymerization mechanism. Furthermore, MPC monomers can form charge transfer complexes and release solvated electrons under heating conditions, a phenomenon confirmed by electron paramagnetic resonance (EPR) tests (Figure 2g). This self-initiating process generates a pair of monomer radical intermediates, which then initiates the subsequent polymerization reaction and ultimately leads to gelation. Selecting appropriate liquid solvents for validation of effective component (Figure S10, Supporting Information), real-time in situ Raman monitoring (Figure 2h) confirmed significant C═C peak attenuation and polymerization progress over 2 h at 80 °C, control experiments with 1-hexyl-3-methylimidazolium chloride (HMImCl) excluded ChCl's catalytic role. Notably, MPC in DES undergoes spontaneous polymerization even at low concentrations (Figure S11a, Supporting Information), indicating that low concentrations are sufficient for gelation under these conditions. As illustrated in Figure S11b (Supporting Information), the final conversion of MPC consistently exceeds 75% across all tested temperatures within 200 mins. During this test period, the conversion rates at different temperatures showed significant differences, and the reaction rate also exhibited obvious variations, indicating that the kinetic behaviors were also significantly different. We also conducted a range of HBD-triggered FRP at various temperatures and calculated the activation energy, which was found to be 74.6 kJ mol^{-1} (Figure S11c,d and Table S2, Supporting Information). These results demonstrate that the DES-based system follows well-defined kinetics and that the hydrogen-bond-assisted mechanism provides a moderate activation energy consistent with efficient polymerization.

Moreover, other zwitterionic monomers, including sulfobetaine methacrylate (SBMA), carboxybetaine methacrylate (CBMA), sulfobetaine acrylamide (SBAA), sulfobetaine vinylimidazole (SBVI), and sulfobetaine vinylpyridine (SBVP), successfully underwent polymerized gelation through supramolecular interactions in Lewis acid-base systems (Figure 2i,j). Replacing urea with other hydrogen-bonding donors, such as glycerol (Gly) or lactic acid (LA), also facilitated polymerization, further demonstrating the versatility of this system (Figure S12, Supporting Information). Rheological analysis of the resultant gels (Figure 2k) showed typical elastic responses across frequencies, with MPC@(ChCl&Gly) exhibiting higher moduli and more pronounced gel characteristics.

2.2. Gel Properties and Electromechanical Decoupling

To improve the mechanical properties of pure zwitterionic eutectogels, hydrogen-bonded microdomains were integrated into the zwitterionic polymer chains through thermally self-initiated polymerization. This process mimics the hierarchical structure of natural skin.[38] The fundamental properties of the copolymer eutectogels, such as their chemical structure, optical characteristics, and environmental stability, were systematically examined. The copolymerization reaction between NAGA and MPC was verified in Gly and monitored via in situ Raman spectroscopy at 80 °C. Since NAGA and MPC were introduced at equal molar masses and the ─C═O band was used as an internal reference, the ─C═C peak of NAGA appeared significantly stronger than that of MPC (Figure S13a, Supporting Information). As the reaction progressed, the ─C═C peak intensity diminished significantly within 1 h (Figure S13b, Supporting Information), indicating near-complete consumption of the ─C═C and thereby providing indirect evidence that random copolymerization had indeed occurred. Figure S13c (Supporting Information) shows the attenuated total reflectance-fourier transform infrared spectroscopy (ATR-FTIR) of eutectogels with different polymer components. After radical polymerization, all eutectogels displayed strong absorption peaks ≈1650 and 1610 cm^{-1}, corresponding to amide groups. Additionally, a broad absorption band at 3329–3195 cm^{-1} indicated multiple hydrogen-bond interactions within the system.

To explore how interactions between amino-formed hydrogen-bonded microdomains and DES respond to temperature, in situ infrared analysis was used. This analysis studied temperature-dependent changes in the ν(C═O) band of amide groups, which are capable of forming hydrogen bonds. As shown in **Figure 3a**, several interaction forms were identified, including free amide groups, solvated amide hydrogen bonds, and multiple amide hydrogen bonds. Heating caused the intensities of dipole-associated and multiple amide hydrogen bonds to decrease, while the intensity of DES–hydrogen-bonded interactions increased, and free ν(C═O) signals appeared. Thermal energy weakened intra-polymer chain interactions, shifting the dipole ν(C═O) (Poly(N-acryloyl glycinamide), PNAGA) to higher wavenumbers. To further clarify these effects, variable-temperature infrared spectra were processed into 2D correlation spectroscopy (2DCOS), which enhanced spectral resolution and revealed the interaction sequence of C═O–associated groups during heating (Figure S14 and Table S3, Supporting Information).[39,40] Both synchronous and asynchronous spectra, reflecting synchronized and unsynchronized intensity changes at given wavenumbers, respectively, revealed the interaction sequence of C═O–associated groups during heating (→ denotes precedence; details in Table S2, Supporting Information): 1624→1580→1700→1687→1665 cm^{-1}, corresponding to ν(C═O) (multiple amide H-bonds, strong dipole) → ν(C═O) (amide H-bonds, weak dipole) → ν(C═O) (free amide groups) → ν(C═O) (solvated amide H-bonds, strong dipole) → ν(C═O) (solvated amide H-bonds, weak dipole). This sequence reflects the progressive weakening and solvation-dependent reorganization of hydrogen-bonded C═O groups during temperature change. 2DCOS allowed us to distinguish between four ν(C═O) conformations in PNAGA and solvent amide groups.

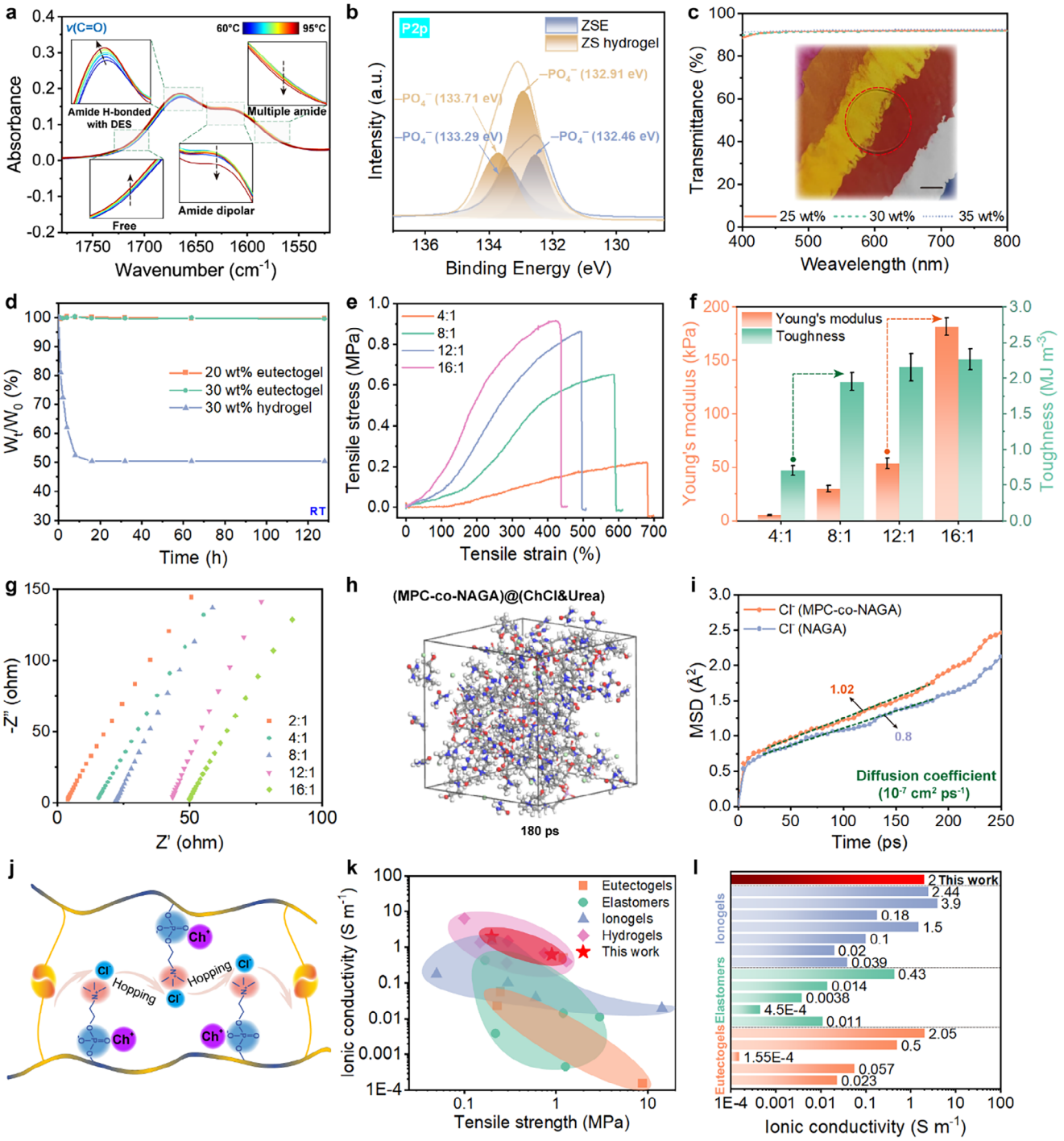

Figure 3. Fundamental properties and electromechanical characterization of the skin-inspired ZSE. a) Temperature-dependent FTIR spectra of ZSE during heating from 60 to 95 °C (5 °C intervals). b) P2p spectra of ZSE and ZS hydrogel. c) Transmittance curves of copolymer gels with varying DES contents (film thickness: 1 mm; inset shows photographs of eutectogels with 30 wt% copolymer content). d) Weight variation of zwitterionic eutectogels and hydrogels over time under ambient conditions (room temperature, 40% RH). e) Tensile stress–strain curves and f) Young's modulus/toughness comparison of ZSE with 30 wt% monomer content at varying molar ratios. g) EIS Nyquist plots of ZSE with varying monomer molar ratios (NAGA:MPC, 30 wt% solid content). h) Representative molecular dynamics simulation (MDS) snapshot of ZSE at 180 ps. i) Mean squared displacement (MSD) curves of dissociated Cl^- ions in PNAGA and P(NAGA–co–MPC) eutectogels. j) Schematic of ion migration mechanisms in zwitterionic eutectogels, highlighting Cl^- hopping via $-N^+(CH_3)_3$ groups. k) Area chart of ionic conductivity and tensile strength against previously reported gels/elastomers. l) Ionic conductivity comparison between skin-like zwitterionic eutectogels and non-hydrogel systems for wearable iontronic sensing.

These findings show that polar groups in DES, such as hydroxyl and amide groups, interact with amide groups in PNAGA, explaining their good compatibility with DES. The earliest dissociation of multiple amide hydrogen bonds also highlights their role in providing thermal recyclability and contributing to the elasticity of the microdomains. Additionally, varying the content of diamide groups showed that pure PNAGA eutectogels had a sharpened diffraction peak at 22.3° and a new peak near 32.1° (Figure S15, Supporting Information), indicating enhanced ordering in gels polymerized solely from NAGA monomers. Atomic force microscopy (AFM) revealed no significant microphase separation in the eutectogels (Figure S16, Supporting Information), confirming nanoscale homogeneity in the ZSE. Compared to pure PNAGA and poly(2-methacryloyloxyethyl phosphorylcholine) (PMPC) eutectogels, pure PMPC showed weaker interchain binding due to ionic interactions, while PNAGA exhibited more pronounced surface undulations from multiple hydrogen-bonded microdomains.

X-ray photoelectron spectroscopy (XPS) and energy-dispersive X-ray spectroscopy (EDS) were also used to investigate ion-dipole interactions and elemental distribution. Figure S17a (Supporting Information) confirms the presence of C, N, O, P, and Cl elements via XPS. Figure S18 (Supporting Information) shows uniform elemental distribution and smooth surfaces, which facilitate dense ion-dipole dynamic bonds that enhance conductivity. High-resolution P2p spectra (Figure 3b) showed shifts in the ionic-state spin-orbit doublets, indicating stronger interactions between quaternary ammonium groups and phosphate groups.[41] Similar shifts were observed in the N1s spectra for quaternary ammonium and amide groups (Figure S17b, Supporting Information), further confirming intensified ion-dipole interactions in ZSE. All eutectogels, regardless of DES content, exhibited high transmittance (over 90%) in the visible range (400–800 nm) and optical transparency (Figure 3c).

To evaluate environmental stability, we compared the weight retention of zwitterionic eutectogels and hydrogels upon air exposure. As shown in Figure 3d, hydrogels lost over 15% of their weight within 2 h and ≈40% within a day. In contrast, eutectogels showed minimal weight loss (0.5%) after one week at room temperature, demonstrating excellent ambient stability. Differential scanning calorimetry (DSC) (Figure S21, Supporting Information) showed no crystallization peaks and revealed glass transition onset temperatures near −70 °C, despite the ChCl&Urea DES exhibiting a crystallization temperature of ≈12 °C.[42] These results indicate excellent thermal stability, even in cryogenic environments. Zwitterionic supramolecular (ZS) hydrogels also exhibited antifreeze properties, as charged groups in zwitterions suppress ice formation via electrostatically induced hydration, consistent with previous studies.[28,43] In addition, the obtained ZSE exhibits acceptable stability in various solvent/solution environments, including polar solvents (such as pure water, tetrahydrofuran, and ethanol), salt water, and a mass fluctuation of less than 3 wt% after soaking in non-polar solvents (such as n-heptane) for 70 h (Figure S22a,b, Supporting Information). The results show that a dense H-bonding network effectively suppresses excessive swelling. However, the gel shows a certain degree of swelling followed by shrinkage in acidic solutions and significant swelling in alkaline solutions (Figure S22c, Supporting Information), which is mainly attributed to the difference in the hydration ability of the zwitterionic groups under different pH conditions after the DES exchange in the solution reaches equilibrium.

The synergy between multi-hydrogen-bonded microdomains and ion-dipole supramolecular interactions is crucial for the mechanical and ionic conductive properties of eutectogels. By adjusting the NAGA/MPC ratio, we controlled hydrogen-bonding sites and zwitterionic group density, balancing crosslinking density and ion mobility. This optimization resulted in eutectogels with skin-like strain-hardening behavior,[44] as seen in Figure 3e and Figure S23a (Supporting Information). The skin-mimetic supramolecular nature of ZSE is also supported by the tensile curves with different stretching rates (Figure S24a, Supporting Information). A higher stretching rate leads to a higher modulus and more pronounced strain–stiffening effect, due to the delayed and sluggish response of chain disassociation.[45] Meanwhile, the differential modulus $\partial\sigma_{true}/\partial\lambda$ also behaves in a similar sigmoid curve to that of the biological tissues (Figure S24b, Supporting Information).[46] Therefore, the hydrogen-bonded clusters and dipole interactions of supramolecular zwitterions are beneficial to realize the biological strain-adaptive phenomenon. The tensile strength increased as the NAGA molar content rose, while the fracture strain decreased. Eutectogels with higher NAGA content (e.g., 8:1 and 12:1 ratios) exhibited enhanced strength and toughness, and their mechanical properties became more skin-like, with both Young's modulus and toughness increasing accordingly. (Figure 3f; Figure S23b, Supporting Information). The high elasticity and fatigue resistance of the synthesized eutectogel were further verified through continuous cyclic tensile tests conducted at 100% strain for 1000 cycles (Figure S23c,d, Supporting Information).

Ionic conductivity was influenced by the size of ion channels and the number of free ions. When the ion concentration in the DES remained constant, the number of mobile free ions was nearly unchanged. In such cases, the ionic conductivity of polymer gels can be enhanced by polymer chain-assisted ion migration.[20] As shown in Figure 3g and Figure S27a (Supporting Information), reducing the NAGA:MPC ratio from 4:1 to 2:1 increased ionic conductivity from 2 to 22 S m^{-1}, although this was accompanied by a reduction in mechanical properties. The ionic conductivity of eutectogels decreased with an increase in copolymer concentration (Figures S27b,c and S28a,b, Supporting Information), as stronger hydrogen bonds and denser dipole crosslinking hindered ion migration. Compared to ZS hydrogels at similar polymer concentrations (Figure S28c,d, Supporting Information), ZSE exhibited more than five times higher ionic conductivity after environmental equilibration, emphasizing the role of conductive DES in boosting ionic conductivity.

Temperature-dependent conductivity trends (Figure S29, Supporting Information) showed two distinct regimes: a gradual decrease in conductivity above 18 °C and a faster decline below this temperature. Conductivity followed a linear relationship with inverse temperature, allowing us to calculate activation energy using the Arrhenius law.[47] The activation energy decreased as the zwitterionic monomer content increased, correlating with higher conductivity (Table S4, Supporting Information).[48] DFT calculations revealed that zwitterionic chain–counterion pairs facilitated the dissociation of Cl^- and Ch^+ in the DES (Figure S30a, Supporting Information). Molecular dynamics simulations (MDS)

confirmed that zwitterionic chain counterions promoted the dissociation of ions in DES, enhancing ion mobility (Figure 3h,i; Figure S30b–d, Supporting Information). The proposed migration mechanism involves Cl^- ions hopping through zwitterionic cationic channels. (Figure 3j). Overall, the eutectogels developed here exhibit superior mechanical properties and ionic conductivity (Figure 3k),[5,7,24,28,49–64] making them ideal for wearable or interfacial iontronic sensing applications (Figure 3l).[5,7,24,49–59,65–67]

2.3. Sensing Interface Applications

Various methods have been explored to create continuous eutectogel filaments from non-spinnable monomer solutions,[53,68] aiming to enhance the diverse and multifunctional properties of self-initiating eutectogels. However, the limited mold length has hindered continuous spinning. **Figure 4**a shows the coaxial wet spinning-thermal reaction strategy used to fabricate zwitterionic supramolecular eutectogel filaments (ZSEF). This rapid extrusion process allows for the production of spooled eutectogel filaments, showing promise for large-scale production of ionically conductive filaments (Figure 4b). To achieve filaments with high mechanical strength and conductivity, the molar ratio of NAGA to MPC in ZSE was set to 12:1, with a 30 wt% mass percentage. The ZSEF could be stretched up to 100% strain and recovered quickly (Figure 4c). It can also support a weight of 200g (Figure 4d), indicating its potential for wearable strain sensors in textiles. The filament diameter is primarily determined by the inner diameter of the coaxial needle tip, resulting in filaments ≈800 µm in thickness (Figure S31, Supporting Information). After 500 stretch/release cycles, scanning electron microscopy (SEM) images revealed no significant cracks, and the filaments maintained smooth surfaces (Figure 4e).

To evaluate their elastic recovery, we conducted cyclic tensile and compressive tests. Energy dissipation and hysteresis primarily result from chain entanglements, disentanglement, and internal friction between polymer chains. Significant hysteresis was observed at high strains (50–250%) in the tensile curves (Figure S32a, Supporting Information). Figure 4f shows the tensile recovery cycle at 100% strain, with ≈10% residual strain upon unloading, but the strain quickly recovered after 2 min. Similar recovery was seen at 200% strain (Figure S32b, Supporting Information). The elastic recovery coefficient at 100% strain was above 92%, confirming excellent performance (Figure 4g). In compression, the stress–strain curves after one cycle nearly overlapped, showing minimal variation and a recovery coefficient of 95% (Figure S33, Supporting Information). These results demonstrate that ZSEF maintains excellent elasticity under low strain due to double-hydrogen-bonded microdomains.

We used polarized optical microscopy (POM) to visualize the rapid recovery of these microdomains, revealing changes in filament orientation under stress. Polarization images at 45° and −45° angles showed color gradients that indicated the filament's alignment direction (Figure 4h). The differences in color intensity were more noticeable at 50% and 100% strain compared to 200%, likely due to internal friction from chain disentanglement (Figure S34, Supporting Information). Additionally, the eutectogel network's non-covalent interactions and water-mediated sol-gel transition make ZSEF recyclable (Figure 4i). Heating dissociates hydrogen bonds and dipole interactions, dissolving the ZSEF into a sol state, and water removal allows the polymer chains to rearrange and form new hydrogen bonds, demonstrating recyclability (Figure S38a, Supporting Information). After several recycling cycles, mechanical properties remained stable (Figure S38b, Supporting Information).

ZSEF's mechanical flexibility and ionic conductivity make it ideal for wearable motion sensing and physiological monitoring (Figure S39, Supporting Information). Stretching the gel filament causes deformation of the polymer chains and contraction of the ion migration channels, which in turn affects the diffusion behavior and migration ability of the conductive ions, leading to an increase in resistance with strain (Figure 4j).[69] A linear relationship between resistance change ($\Delta R/R_0$) and strain (<100%) was observed, with a gauge factor (GF) of 1.28. This implies that the fabricated ZSEF exhibited outstanding sensitivity across low-strain ranges, which is attributed to the robust hydrogen-bonded clusters that can faithfully transfer stress to the internal molecular backbone.[70] The ZSEF-based strain sensor showed fast response (338 ms) and recovery (305 ms) (Figure 4k). When strain is applied, the ionic conduction pathways within the gel dynamically reorganize due to the reorientation of zwitterionic groups and reversible hydrogen bonding interactions. Upon unloading, these supramolecular interactions rapidly recover, enabling rapid and reversible electrical responses.[71] Minimal hysteresis at 150% strain further confirmed reliable resistance–strain behavior (Figure 4l). Real-time resistance monitoring across strains of 0–200% revealed dynamic responses in both low (1–50%) and high (100–200%) ranges (Figure 4m; Figure S40, Supporting Information). The sensors also demonstrated stable performance across varying stretching rates and over 500 cycles at ≈50% strain (Figures S41 and S42, Supporting Information), even under 100% and 200% strain holding (Figure S43, Supporting Information).

To demonstrate the sensing capabilities, we embedded two ZSEFs into a cotton glove, allowing for anisotropic sensing along the warp and weft directions (Figure 4n). The ZSEF sensors could independently detect strain signals from fist-clenching motions at −20 °C, and different finger postures generated unique electrical signals for gesture monitoring (Figure S44, Supporting Information). Using these signals, we demonstrated the ability to transmit distress signals in Morse code, such as "DHU," "SOS," and "HELP," showing that ZSEF sensors can be integrated into electronic textiles for extreme environments (Figure S46, Supporting Information; Figure 4o).

Epidermal bioelectronics require stable adhesion for accurate signal collection. In this study, MPC was used as the adhesive component in ZSE, strengthening the adhesive properties by increasing its content. This, combined with carbon cloth electrodes, enabled the creation of epidermal zwitterionic supramolecular eutectogel patches (ZSEP) (**Figure 5**a). The ZSEP gel shows strong adhesion to various materials, including poly(methyl methacrylate) (PMMA), polyethylene/polypropylene (PE/PP), polytetrafluoroethylene (PTFE), glass, rubber, and skin (Figure S50a, Supporting Information). It also strongly bonds to metals like copper and aluminum and exhibits excellent adhesion to human skin, even during wrist movements (Figure 5b). Additionally, the gel adheres well to latex balloons during dynamic inflation and deflation (Figure S50b, Supporting Information).

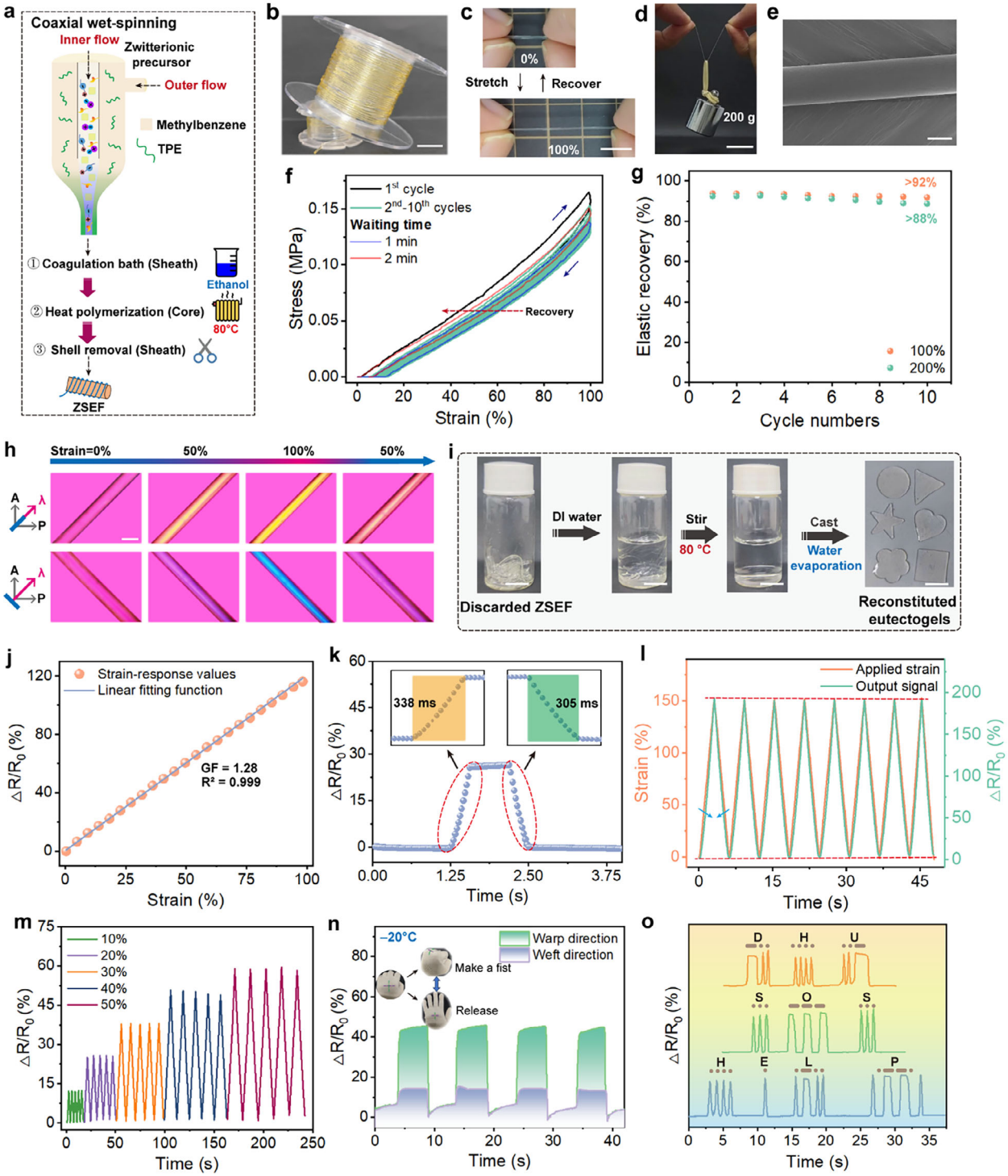

Figure 4. Continuous fabrication of ZSEF and its flexible sensing performance. a) Schematic of the coaxial wet-spinning process for producing ZSEF. Photographs of ZSEF filaments: b) wound on a collector roller (scale bar: 1.5 cm), c) stretched/recovered at 100% strain (scale bar: 1 cm), d) bearing a 200 g weight (scale bar: 3 cm), and e) SEM image of ZSEF (scale bar: 500 μm). f) Cyclic tensile loading–unloading curves at 100% strain with varying waiting times. g) Elastic recovery of ZSEF under varying strains. h) Polarized optical microscopy (POM) images of ZSEF during stretching (0–100%) and recovery under a 530 nm filter at azimuthal angles of 45° and −45° (scale bar: 1 μm). i) Recycled ZSEF via water-mediated sol-gel reprocessing (scale bar: 1 cm). j) Strain sensitivity (0–100%) and k) response/recovery times (20% strain) of the ZSEF sensor. l) Synchronized strain–electrical signal response under stretching (rate: 50 mm min^{-1}). m) Relative resistance change under 10–50% strains (stretching rate: 50 mm min^{-1}). n) Axial and transverse resistance changes of ZSEF sensors during fist clenching/relaxation in a subzero environment (−20 °C), with an anisotropic strain–sensing glove with cross-embedded ZSEF and photographs of hand gestures. o) Morse code outputs of "DHU", "SOS", and "HELP" messages.

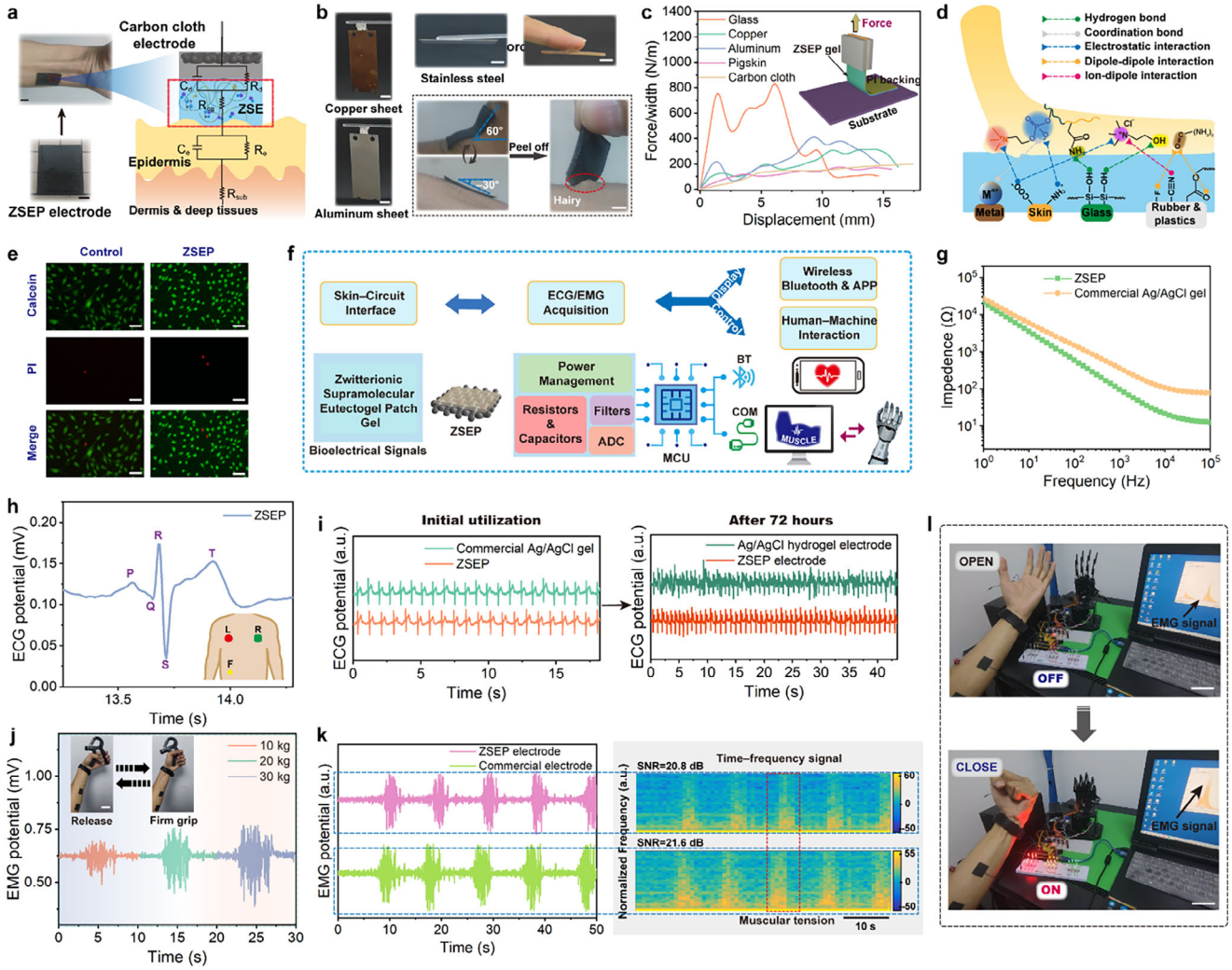

Figure 5. The construction of ZSEP and its application as an interface electrode for physiological signal monitoring and human-machine interaction. a) Equivalent circuit model for ZSEP-based physiological monitoring (electrode platform: R_d: charge transfer resistance, C_d: double-layer capacitance, R_{cg}: ZSE resistance; skin platform: R_e: epidermal resistance, C_e: epidermal capacitance, R_{sub}: dermal/subdermal resistance) (scale bar: 0.5 cm). b) Photographs of ZSEP adhered to copper, aluminum, stainless steel, and human skin, along with adhesion and peeling performance at varying bending angles on hairy wrist skin (scale bar: 0.5 cm). c) Peeling force–displacement curves of ZSEP against different substrates (inset: standard 90° peeling test setup). d) Schematic of adhesion mechanisms between ZSEP and substrates. e) Live/dead cell staining assay of fibroblasts treated with ZSEP extract. f) Key components and signal acquisition/control workflow of the ZSEP biosensor. g) Interfacial impedance spectra comparison between ZSEP and commercial Ag/AgCl gel electrodes. h) Representative ECG signals recorded by ZSEP electrodes (inset: schematic of three-electrode placement on the human body). i) ECG signals acquired by ZSEP and commercial Ag/AgCl gel electrodes after 72 h of intermittent wearing on human skin. j) EMG signals under varying grip strengths (inset: photographs of gripping and releasing a hand grip strengthener; scale bar: 4 cm). k) EMG signals and spectral analysis profiles obtained by ZSEP and commercial electrodes. l) ZSEP electrode-acquired EMG signals driving robotic hand actuation and LED bulb switching via MCU, with real-time EMG image signals displayed on-screen (scale bar: 4 cm).

Standard 90° peel testing further quantified ZSEP's substrate adhesion strength. Figure 5c reveals substantial peeling forces across all tested substrates, with the gel exhibiting maximum adhesion to glass (750 N m^{-1}), followed by metals (aluminum and copper), porcine skin, and conductive carbon cloth fabrics (all below 200 N m^{-1})—properties favorable for wearable soft iontronics. ZSEP's exceptional adhesion stems from both adhesive interactions at the interface, combined with tough hydrogen-bonded domains that redistribute energy during peeling (Figure 5d).[72,73] In vitro biocompatibility assessment of ZSEP gel demonstrated that the survival rate of L929 cells exposed to high-concentration extracts for 3 days still exceeded the safety standard (>75%), confirming the material's safety (Figure S52, Supporting Information). Live/dead cell staining via confocal laser scanning microscopy (CLSM) after three days of culture further validated the safety of direct contact to the human body (Figure 5e). Meanwhile, the gel exhibited ≈100% antibacterial efficiency against both Gram-negative (*E. coli*) and Gram-positive (*S. aureus*) bacteria (Figure S53, Supporting Information). The antibacterial mechanism is attributed to the ChCl quaternary ammonium groups in the DES system, which disrupt the bacterial membrane structure through electrostatic interaction.[74]

To enable physiological signal monitoring and human-machine interaction, we developed a wireless electrocardiogram (ECG) health monitoring and wired electromyogram (EMG) feedback control platform (Figure 5f). This platform uses the ZSEP gel as an interfacial electrode, offering low contact impedance for ECG signal collection (Figure 5g). The ZSEP electrodes showed lower skin–electrode interface impedance than commercial Ag/AgCl electrodes, and successfully captured ECG signals, as demonstrated by periodic PQRST waveforms (Figure 5h). ZSEP's environmental stability ensures long-term, high-fidelity ECG monitoring, even under low-humidity conditions (Figure 5i; Figure S57, Supporting Information). Furthermore, Figure S55 (Supporting Information) illustrates accurate wireless ECG recording using ZSEP–A&B electrodes integrated with a BMD101 device on the chest. Additionally, ZSEP electrodes successfully captured EMG signals from muscle contractions, demonstrating the potential for human-computer interaction applications (Figure 5j). The electrodes' performance remains stable after 24–48 h of storage, highlighting their superior signal stability and retention compared to commercial electrodes (Figure 5k; Figure S58, Supporting Information).

These results demonstrate the feasibility of ZSEP electrodes for high-quality signal acquisition and interactive control, making them suitable for wearable bioiontronics and advanced monitoring applications,[75] such as robotic hand control and EMG-based muscle activity analysis (Figure S59, Supporting Information). The dual-channel EMG collection system enables stepwise control of palm movement and arm rotation, illustrating the potential of ZSEP electrodes in complex robotic manipulations (Figure 5l).

3. Conclusion

In this study, we developed a versatile spontaneous PDES system, demonstrating a novel approach to create bioinspired soft materials with both mechanical resilience and high ionic conductivity. The ZSE, synthesized based on Lewis acid-base interactions, successfully mimics the dynamic characteristics of human skin through an environmentally friendly gelation method that does not require initiators or crosslinkers, highlighting its potential applications in wearable biointerfaces. Integration of hydrogen-bonded microdomains with ion-dipole interactions enhances mechanical and ionic properties, enabling real-time motion and physiological signal monitoring. Additionally, we demonstrated the scalability of ZSEF and its advantage in wearable sensing. The development of ZSEP further expands its application in epidermal iontronics, offering stable adhesion, low contact impedance, and excellent performance under extreme conditions. This work provides a sustainable, scalable synthesis platform for the fabrication of multifunctional ionic gels with significant potential for advanced wearable bioiontronics and soft robotics, bridging synthetic gels with the biological structure and ion-regulatory functions of skin.

4. Experimental Section

Synthesis of DESs and ZSE: To prepare the DES, HBA ChCl (13.96 g, 0.1 mol) and HBD urea (12.01 g, 0.2 mol) were mixed at a 1:2 molar ratio, heated with stirring at 80 °C until a clear liquid formed, and cooled to room temperature while maintaining a transparent liquid state. DESs containing different HBDs (Gly (18.42 g, 0.2 mol) or LA (18.02 g, 0.2 mol)) were prepared using the same procedure.

Subsequently, NAGA (PHBD) and MPC (PZHBA) were added at varying molar ratios to the DES (ChCl&Urea), heated with stirring at 50 °C until dissolved, and quickly transferred to PTFE or glass molds. The molds were placed in a vacuum oven at specific temperatures for a defined period to synthesize ZSE. The resulting ZSE was removed and equilibrated for 48 h under controlled temperature and humidity (RT = 25 °C, RH = 80%). Additionally, pure zwitterionic eutectogels with different compositions were prepared using similar methods (detailed formulations in Tables S5 and S6, Supporting Information). As controls, PNAGA eutectogel (30 wt%) and ZS hydrogel (30 wt%, NAGA:MPC = 8:1) were synthesized via UV initiation. Briefly, photoinitiator I2959 (0.1 wt% of monomer mass) was added to the DES or aqueous monomer mixture, and the precursor solution was irradiated with a UV lamp (90 W, 365 nm) for 15 min to initiate polymerization, yielding ZSE.

Preparation of ZSEF and Sensing Tests: ZSEF was fabricated via a coaxial wet-spinning thermal reaction strategy. For the shell spinning solution, 10 g TPE was dissolved in 20 g toluene and stirred uniformly at room temperature. The core spinning solution utilized ultrasonically degassed ZSE precursor (monomer molar ratio adjusted to NAGA:MPC = 12:1). Coaxial encapsulation and thermal reaction were performed using a coaxial needle with a 21G inner channel (the other two types use the inner channels of size 19G and 23G) and 17G outer channel. The shell solution was extruded into an ethanol coagulation bath through the outer channel at 100 µL min^{-1}, rapidly forming hollow thermoplastic elastomer (TPE) microtubes. Simultaneously, the core precursor was injected into the inner channel at 50 µL min^{-1} to form the central core filament. Finally, in situ thermally initiated self-polymerization of the core precursor was achieved by fully heat-treating the coaxial filament at 80 °C for 1 h. The sheath layer was easily removed by swelling in ethyl acetate, yielding the final ZSEF.

For sensing tests, ZSEF served as a conductor. Copper wires were wound at both ends of the gel filaments, with leads extended from each side. The sensor was fixed on a stretching clamp of a universal testing machine (Instron 5967), and resistance changes in ZSEF were monitored using a multimeter (Tektronix DMM7510). The fixture's movement speed was set to 50 mm min^{-1}. Relative resistance changes ($\Delta R/R_0$) were calculated as $\Delta R/R_0 = (R–R_0)/R_0 \times 100\%$, where R_0 and R represent the initial and real-time resistances, respectively. The gauge factor (GF), a key parameter for evaluating sensitivity, was calculated as $GF = (\Delta R/R_0)/\epsilon$ (ϵ: applied strain). ZSEF-based woven embedded sensors enabled real-time monitoring of resistance changes corresponding to human body motions (knee bending, finger flexion, elbow bending, pulse, etc.), with data acquisition methods varying across application scenarios. Temperature response behavior was tested using a heating stage equipped with a temperature monitoring unit.

Preparation of ZSEP Electrodes and Their Interfacing Applications: ZSEP electrodes were prepared by adjusting the monomer molar ratio to NAGA:MPC = 4:1, uniformly coating ZSE precursor onto conductive carbon cloth, and performing rapid in situ thermally initiated self-polymerization. The resulting ZSEP was cut into 2 × 1.5 cm^2 rectangular electrodes and connected to testing devices. The interfacial contact impedance of ZSEF gel was measured using an electrochemical workstation (Vertex C, IVIUM Tech, Netherlands) with a 0.1 V applied potential and frequency range of 0.1–10^5 Hz. Biosignal detection with ZSEP electrodes:

1) ECG: Signals were acquired using a commercial AD8232 device (Sichiray Technology). Working electrodes were placed on the left and right chest, and the reference electrode on the lower left abdomen. ECG was also recorded via ZSEP electrodes integrated with a wireless acquisition system (BMD101). ZSEP electrodes attached to the chest skin transmitted real-time ECG data to a smartphone via Bluetooth.
2) EMG: MyoWare sensors with three-electrode configurations (sampling frequency: 500 Hz) were used. ZSEP electrodes were placed 2 cm apart on the forearm flexor muscles, with the reference electrode at the

elbow. Commercial electrodes were placed at identical positions to eliminate positional signal variations. EMG data were processed in MATLAB for spectral analysis. Signal–noise ratio (SNR) was calculated as $SNR = 20 \times \log_{10}(P_{signal}/P_{noise})$, where P_{signal} and P_{noise} represent the potential of the signal and background, respectively. Values were determined via root mean square (RMS) analysis (noise band: 10–30 Hz), indicating the variation of the signal over time.

3) Interactive control: Bandpass-filtered EMG signals were processed by an ATmega328P microcontroller and converted into control signals for a robotic hand (uHand, Hiwonder) and LED lights. Arduino control programs were coded in C++.

All participants provided prior written informed consent. Epidermal bioelectronic applications were tested on the first author after passing biocompatibility and skin irritation assessments. This study was approved by the Ethics Review Committee of Donghua University.

Instrumentation: ^{1}H NMR spectra were recorded on a Bruker AV-400 spectrometer using D_2O or DMSO-d_6 as solvents. The relative molecular weights of synthesized polymers were determined via GPC (Agilent 1260) with water as the mobile phase (flow rate: 1 mL min^{-1}, room temperature). SEM and EDS images were acquired on a Hitachi SU8010. Surface elemental valence states and bonding information were analyzed by XPS (Escalab 250Xi). ATR-FTIR spectra (4000–650 cm^{-1}, resolution: 4 cm^{-1}) were collected on a Nicolet Nexus 670 spectrometer with an ATR accessory to verify chemical structures. Raman spectra were obtained using a multifunctional confocal Raman microscope (RTS2) with a 532 nm laser (80% intensity, measurement range: 4250–125 cm^{-1}). In situ Raman spectroscopy coupled with a temperature-controlled stage was employed to monitor gelation dynamics. Optical properties were evaluated via transmittance measurements (400–800 nm) on a UV–vis–NIR spectrophotometer (Shimadzu UV–3600). UV–vis spectra of reaction solutions were recorded on a Lambda 35 spectrometer. Gel filament diameters and self-healing visual effects were observed using an optical microscope (Nikon SMZ745T). Polarized optical images of gel filaments were captured with an Olympus SZX7 microscope equipped with a 532 nm filter. X-ray diffraction (XRD) analysis was performed on a Bruker D8 ADVANCE with Cu-Kα radiation (λ = 1.5418 Å, 2θ range: 10°–85°, scan rate: 10° min^{-1}). Phase images and microphase structures of gel films were scanned in non-contact mode using an AFM (MFP3D Bio, Oxford Instruments). Small-angle X-ray scattering (SAXS) data were collected on a Xeuss 3.0 system (Cu-Kα radiation: λ = 0.154 nm) with a semiconductor detector (Pilatus 3R 300K), followed by background subtraction and normalization. Antifreeze performance was assessed via DSC (Q250, TA Instruments) under N_2 (20 to −85 °C, cooling rate: −5 °C min^{-1}). Thermogravimetric analysis (TGA, Mettler Toledo) was conducted under N_2 (50–500 °C, heating rate: 10 °C min^{-1}). Stress relaxation (150% strain) and tensile tests were performed on a TA Q800 dynamic mechanical analyzer (DMA) in stretch mode. Solvent retention capacity (η) was calculated as $\eta = (W_t/W_0) \times 100\%$, where W_t and W_0 represent the weights of the gel after and before moisture exchange under controlled humidity/temperature.

Supporting Information

Supporting Information is available from the Wiley Online Library or from the author.

Acknowledgements

B.Z. and Y.L. contributed equally to this work. This work was financially supported by Professor Guo's group (Bionic Functional Textiles Laboratory for Smart Wearable), the Research Platform for Biomedical and Health Technology, NUS (Suzhou) Research Institute (RP-BHT-Prof. LEE Chengkuo), NUS College of Design and Engineering (CDE)-Robotics Seed Grant Programme, "AI-Sensor Enhanced Medical Operation Training System (A-8003283-00-00)", and NUS College of Design and Engineering (CDE)-Robotics Seed Grant Programme, "A Multimodal Sensing/Haptic System for Lower-Limb Exoskeleton Feedback Control (A-8003281-00-00)". The authors also thank Zhiliang Han from College of Materials Science and Engineering of Donghua University for guidance on rheological testing, Xiangnan Yuan from Textile Testing Center of Donghua University for assistance in antibacterial activity test, and Cheng Fang from Textile College of Donghua University for assistance in biocompatibility testing.

Conflict of Interest

The authors declare no conflict of interest.

Data Availability Statement

The data that support the findings of this study are available from the corresponding author upon reasonable request.

Keywords

iontronic interface, initiator-free polymerization gelation, supramolecular zwitterionic gel, skin-mimetic, wearable sensing

Received: July 21, 2025
Revised: November 12, 2025
Published online:

[1] X. Zhang, D. Li, X. Yang, L. Wang, G. Li, T.-W. Wong, T. Li, W. Yang, Z. Luo, *Science* **2025**, *387*, 967.
[2] S. Guo, S. Zhang, H. Li, S. Liu, J. J. Koh, M. Zhou, Z. Sun, Y. Liu, H. Qu, Z. Yu, Y. Zhang, L. Yang, W. Chen, C. He, C. Lee, D. Mao, S. K. Ravi, Y. Lai, S. C. Tan, *Matter* **2025**, *8*, 101785.
[3] C. Lee, Y. Qin, Y.-C. Wang, *MRS Bull.* **2025**, *50*, 428.
[4] X. Guo, Z. Sun, Y. Zhu, C. Lee, *Adv. Mater.* **2024**, *36*, 2406778.
[5] K. Xue, C. Shao, J. Yu, H. Zhang, B. Wang, W. Ren, Y. Cheng, Z. Jin, F. Zhang, Z. Wang, R. Sun, *Adv. Funct. Mater.* **2023**, *33*, 2305879.
[6] T. Liu, Q. Wu, H. Liu, X. Zhao, X. Yi, J. Liu, Z. Nong, B. Zhou, Q. Wang, Z. Liu, *Nat. Commun.* **2025**, *16*, 3334.
[7] Y. Cao, Y. J. Tan, S. Li, W. W. Lee, H. Guo, Y. Cai, C. Wang, B. C.-K. Tee, *Nat. Electron.* **2019**, *2*, 75.
[8] J. Yang, L. Chang, H. Deng, Z. Cao, *ACS Nano* **2024**, *18*, 18980.
[9] M. Wang, X. Xiao, S. Siddika, M. Shamsi, E. Frey, W. Qian, W. Bai, B. T. O'Connor, M. D. Dickey, *Nature* **2024**, *631*, 313.
[10] W. Li, X. Wang, Z. Liu, X. Zou, Z. Shen, D. Liu, L. Li, Y. Guo, F. Yan, *Nat. Mater.* **2024**, *23*, 131.
[11] J. Ma, Y. Lin, Y.-W. Kim, Y. Ko, J. Kim, K. H. Oh, J.-Y. Sun, C. B. Gorman, M. A. Voinov, A. I. Smirnov, J. Genzer, M. D. Dickey, *ACS Macro Lett.* **2019**, *8*, 1522.
[12] M. Wang, P. Zhang, M. Shamsi, J. L. Thelen, W. Qian, V. K. Truong, J. Ma, J. Hu, M. D. Dickey, *Nat. Mater.* **2022**, *21*, 359.
[13] H. Zhou, W. Zhao, L. Zhao, *Chem. Eng. J.* **2024**, *489*, 151163.
[14] L. Meyer, M. B. Andersen, S. Kara, *Angew. Chem., Int. Ed.* **2022**, *61*, 202203823.
[15] D. Dong, C. Tsao, H.-C. Hung, F. Yao, C. Tang, L. Niu, J. Ma, J. MacArthur, A. Sinclair, K. Wu, P. Jain, M. R. Hansen, D. Ly, S. G. Tang, T. M. Luu, P. Jain, S. Jiang, *Sci. Adv.* **2021**, *7*, abc5442.
[16] Z. Lei, P. Wu, *Nat. Commun.* **2018**, *9*, 1134.
[17] S. Y. Zheng, S. Mao, J. Yuan, S. Wang, X. He, X. Zhang, C. Du, D. Zhang, Z. L. Wu, J. Yang, *Chem. Mater.* **2021**, *33*, 8418.
[18] N. Zhao, W. Yuan, *Compos. Part B Eng.* **2022**, *230*, 109525.
[19] X. Peng, H. Liu, Q. Yin, J. Wu, P. Chen, G. Zhang, G. Liu, C. Wu, Y. Xie, *Nat. Commun.* **2016**, *7*, 11782.

[20] J. Yang, Z. Xu, J. Wang, L. Gai, X. Ji, H. Jiang, L. Liu, *Adv. Funct. Mater.* **2021**, *31*, 2009438.
[21] K. He, P. Cai, S. Ji, Z. Tang, Z. Fang, W. Li, J. Yu, J. Su, Y. Luo, F. Zhang, T. Wang, M. Wang, C. Wan, L. Pan, B. Ji, D. Li, X. Chen, *Adv. Mater.* **2024**, *36*, 2311255.
[22] X. Lu, Z. Mo, Z. Liu, Y. Hu, C. Du, L. Liang, Z. Liu, G. Chen, *Angew. Chem., Int. Ed.* **2024**, *63*, 202405357.
[23] R. Liu, T. Wang, G. Li, Z. Fan, Q. Zhou, K. Wang, P. Li, W. Huang, *Adv. Funct. Mater.* **2023**, *33*, 2214917.
[24] W. Zhang, B. Wu, S. Sun, P. Wu, *Nat. Commun.* **2021**, *12*, 4082.
[25] S. Hao, Z. Chen, H. Li, J. Yuan, X. Chen, A. Sidorenko, J. Huang, Y. Gu, *Small* **2024**, *20*, 2309931.
[26] G. Du, Y. Shao, B. Luo, T. Liu, J. Zhao, Y. Qin, J. Wang, S. Zhang, M. Chi, C. Gao, Y. Liu, C. Cai, S. Wang, S. Nie, *Nano-Micro Lett.* **2024**, *16*, 170.
[27] C. Lu, X. Wang, Y. Shen, S. Xu, C. Huang, C. Wang, H. Xie, J. Wang, Q. Yong, F. Chu, *Adv. Funct. Mater.* **2024**, *34*, 2311502.
[28] Y. Yin, R. Xie, Z. Sun, T. Jiang, B. Zhou, Y. Yu, H. Ding, S. Gai, P. Yang, *Nano Lett.* **2024**, *24*, 5351.
[29] Z. Li, H. Xu, Z. Deng, B. Guo, J. Zhang, *Nano Today* **2024**, *59*, 102469.
[30] Z. Sun, Y. Hu, W. Wei, Y. Li, Q. Zhang, K. Li, H. Wang, C. Hou, *Adv. Mater.* **2024**, *36*, 2310102.
[31] W. Zhao, H. Zhou, Y. Lu, J. Jiang, L. Zhao, *Cell Rep. Phys. Sci.* **2024**, *5*, 102107.
[32] Q. He, G. Fang, Z. Chang, Y. Zhang, S. Zhou, M. Zhou, S. Chai, Y. Zhong, G. Cao, S. Liang, A. Pan, *Nano-Micro Lett.* **2022**, *14*, 93.
[33] G. Li, X. Guan, A. Wang, C. Wang, J. Luo, *Energy Storage Mater.* **2020**, *24*, 574.
[34] X. Huang, C. Chen, X. Ma, T. Zhu, W. Ma, Q. Jin, R. Du, Y. Cai, M. Zhang, D. Kong, M. Wang, J. Ren, Q. Zhang, X. Jia, *Adv. Funct. Mater.* **2023**, *33*, 2302846.
[35] S. M. Banik, A. Levina, A. M. Hyde, E. N. Jacobsen, *Science* **2017**, *358*, 761.
[36] Y. Bai, H. Wang, J. He, Y. Zhang, *Angew. Chem., Int. Ed.* **2020**, *59*, 11613.
[37] S. Aoshima, S. Kanaoka, *Chem. Rev.* **2009**, *109*, 5245.
[38] J. Wang, B. Wu, P. Wei, S. Sun, P. Wu, *Nat. Commun.* **2022**, *13*, 4411.
[39] S. Morita, H. Shinzawa, I. Noda, Y. Ozaki, *Appl. Spectrosc.* **2006**, *60*, 398.
[40] Z. Lei, P. Wu, *ACS Nano* **2018**, *12*, 12860.
[41] I. Phiri, C. Y. Bon, S. Kim, M. Mwemezi, L. Hamenu, A. Madzvamuse, S. H. Kim, J. M. Ko, *Curr. Appl. Phys.* **2020**, *20*, 122.
[42] A. P. Abbott, G. Capper, D. L. Davies, R. K. Rasheed, V. Tambyrajah, *Chem. Commun.* **2003**, 70.
[43] Q. Fu, S. Hao, L. Meng, F. Xu, J. Yang, *ACS Nano* **2021**, *15*, 18469.
[44] J. Cui, R. Xu, W. Dong, T. Kaneko, M. Chen, D. Shi, *ACS Appl. Mater. Interfaces* **2023**, *15*, 48736.
[45] Y. J. Tan, H. Godaba, G. Chen, S. T. M. Tan, G. Wan, G. Li, P. M. Lee, Y. Cai, S. Li, R. F. Shepherd, J. S. Ho, B. C. K. Tee, *Nat. Mater.* **2020**, *19*, 182.
[46] M. Vatankhah-Varnosfaderani, A. N. Keith, Y. Cong, H. Liang, M. Rosenthal, M. Sztucki, C. Clair, S. Magonov, D. A. Ivanov, A. V. Dobrynin, S. S. Sheiko, *Science* **2018**, *359*, 1509.
[47] L. Liu, X. Wu, T. Li, *J. Power Sources* **2014**, *249*, 397.
[48] T. Zhou, X. Gao, B. Dong, N. Sun, L. Zheng, *J. Mater. Chem. A* **2016**, *4*, 1112.
[49] X. Lyu, H. Zhang, S. Yang, W. Zhan, M. Wu, Y. Yu, Z. Shen, Z. Zou, *ACS Appl. Mater. Interfaces* **2023**, *15*, 31888.
[50] Y. Liang, K. Wang, J. Li, H. Wang, X. Q. Xie, Y. Cui, Y. Zhang, M. Wang, C. Liu, *Adv. Funct. Mater.* **2021**, *31*, 2104963.
[51] Q. Lu, H. Li, Z. Tan, *ACS Appl. Mater. Interfaces* **2023**, *15*, 34055.
[52] J. Liu, L. Zhou, P. Zhang, Y. Zhao, H. Wei, Y. Yu, *CCS Chem* **2024**, *6*, 390.
[53] L. Zhao, B. Wang, Z. Mao, X. Sui, X. Feng, *Chem. Eng. J.* **2022**, *433*, 133500.
[54] W. Qiu, C. Zhang, Q. Zhang, *ACS Appl. Mater. Interfaces* **2022**, *14*, 42578.
[55] C. Dang, F. Peng, H. Liu, X. Feng, Y. Liu, S. Hu, H. Qi, *J. Mater. Chem. A* **2021**, *9*, 13115.
[56] F. Ou, T. Xie, X. Li, Z. Zhang, C. Ning, L. Tuo, W. Pan, C. Wang, X. Duan, Q. Liang, W. Gao, Z. Li, S. Zhao, *Mater. Horiz.* **2024**, *11*, 2191.
[57] R. Li, G. Chen, T. Fan, K. Zhang, M. He, *J. Mater. Chem. A* **2020**, *8*, 5056.
[58] L. Li, W. Li, X. Wang, X. Zou, S. Zheng, Z. Liu, Q. Li, Q. Xia, F. Yan, *Angew. Chem., Int. Ed.* **2022**, *61*, 202212512.
[59] Y. Cheng, H. Zhu, S. Li, M. Xu, T. Li, X. Yang, H. Song, *ACS Sustainable Chem. Eng.* **2023**, *11*, 15031.
[60] Y. Chen, C. Zhang, R. Yin, M. Yu, Y. Liu, Y. Liu, H. Wang, F. Liu, F. Cao, G. Chen, W. Zhao, *Mater. Horiz.* **2023**, *10*, 3807.
[61] T. Lei, Y. Wang, Q. Zhang, H. Wang, X. Duan, J. Yan, Z. Xia, R. Wang, W. Shou, X. Li, J. Fan, *Nano Energy* **2024**, *126*, 109633.
[62] W. Zhao, H. Zhou, W. Li, M. Chen, M. Zhou, L. Zhao, *Nano-Micro Lett.* **2024**, *16*, 99.
[63] H. Wei, Z. Wang, H. Zhang, Y. Huang, Z. Wang, Y. Zhou, B. B. Xu, S. Halila, J. Chen, *Chem. Mater.* **2021**, *33*, 6731.
[64] X. Dang, Y. Fu, X. Wang, *Biosens. Bioelectron.* **2024**, *246*, 115893.
[65] J. Yang, Y. Feng, B. Wang, J. Miao, S. Wei, H. Li, L. Mo, Z. Qin, *Chem. Eng. J.* **2023**, *474*, 145544.
[66] B. Zhao, J. Yan, F. Long, W. Qiu, G. Meng, Z. Zeng, H. Huang, H. Wang, N. Lin, X. Liu, *Adv. Sci.* **2023**, *10*, 2300857.
[67] N. Li, Y. Qiu, J. Ma, L. Qiu, W. Sun, J. Li, Z. Han, W. Chen, X. Ji, *ACS Appl. Polym. Mater.* **2023**, *5*, 9974.
[68] X. Wang, G. Chen, L. Cai, R. Li, M. He, *ACS Appl. Mater. Interfaces* **2021**, *13*, 8952.
[69] S. Liu, Y. Li, J. Wen, Z. Shen, Q. Meng, Q. Liu, F. Yang, S. Yu Zheng, J. Li, Z. Sun, G. Zhuang, J. Yang, *Adv. Funct. Mater.* **2024**, *34*, 2313397.
[70] Z. Wang, D. Wang, D. Liu, X. Han, X. Liu, H. Torun, Z. Guo, S. Duan, X. He, X. Zhang, B. B. Xu, F. Chen, *Adv. Funct. Mater.* **2023**, *33*, 2301117.
[71] Z. Wu, L. Zhang, M. Wang, D. Zang, H. Long, L. Weng, N. Guo, J. Gao, Y. Liu, B. B. Xu, *Adv. Compos. Hybrid Mater.* **2024**, *8*, 17.
[72] M. Gao, H. Wu, R. Plamthottam, Z. Xie, Y. Liu, J. Hu, S. Wu, L. Wu, X. He, Q. Pei, *Matter* **2021**, *4*, 1962.
[73] M. Guo, G. Li, M. Cai, X. Hou, K. Huang, J. Tang, C. F. Guo, *Nano Lett.* **2023**, *23*, 1371.
[74] H. M. Bedair, T. M. Samir, F. R. Mansour, *Appl. Microbiol. Biotechnol.* **2024**, *108*, 198.
[75] K. Li, J. Zhang, L. Wang, M. Zhang, J. Li, S. Bao, *Biomed. Signal Process. Control* **2020**, *62*, 102074.